MALAYSIAN JOURNAL OF MICROSCOPY

Journal homepage: https://malaysianjournalofmicroscopy.org

RESEARCH ARTICLE

ELECTROCHEMICAL PERFORMANCE OF ANTIMONY-MODIFIED POROUS LAMELLAR ZINC ALLOY ANODE IN ALKALINE AQUEOUS ELECTROLYTE

Muhammad Afiq Irfan Mohd Shumiri[1], Abdillah Sani Mohd Najib[1,2], Nor Akmal Fadil[1,2,*]

[1]Materials Research and Consultancy Group, Faculty of Mechanical Engineering, Universiti Teknologi Malaysia, 81310 Skudai, Johor Bahru, Malaysia.
[2]Department of Materials, Manufacturing and Industrial Engineering, Faculty of Mechanical Engineering, Universiti Teknologi Malaysia, 81310, Skudai, Johor Bahru, Malaysia.

Abstract. Metallic zinc is one of the most attractive anode materials for post-lithium batteries due to its natural abundance, safety, low cost and high theoretical capacity. However, it often suffers from severe polarization and poor reversibility, which hinder the practical application in aqueous alkaline rechargeable zinc-ion batteries. Herein, this work presents antimony-modified porous lamellar zinc anode (Sb-pZn) as a promising high-performance negative electrode. The porous structure was fabricated by chemical dealloying of eutectic Zn-Al alloy, in which the less noble Al component was selectively removed in sodium hydroxide (NaOH) solution. This process produces a well-defined lamellar pattern with aligned porous channels, providing high surface area that facilitates efficient ion transport and enhances electrochemical stability. Surface modification was performed through galvanic replacement reaction in antimony trichloride ($SbCl_3$) solution. This introduces Sb sites that promote uniform Zn nucleation. As a result, Sb-pZn anode with Zn lamellar thickness of ~2920 nm (Sb-pZn-2920) shows improved Zn deposition behavior, with an ultralow nucleation overpotential of 101.3 mV even at high current density of 0.2 mA/cm^2. Cyclic voltammetry shows better redox kinetics with stronger peak currents and reduced peak separation of 0.736 V, while electrochemical impedance spectroscopy confirms a notable decrease in charge transfer resistance from 4.238 Ω for bare Zn to 1.770 Ω for Sb-pZn-2920. The combined effects of Sb incorporation and the tailored porous structure effectively reduce polarization and enhance overall electrochemical performance. This study offers a simple and scalable strategy for developing high-performance Zn anodes and provides valuable insights for advancing next-generation aqueous Zn-based energy storage systems.

Keywords: Zinc anode, surface modification, electrochemical performance, lamellar porous structure.

Article Info

Received 10 January 2026
Accepted 19 April 2026
Published 8 June 2026

***Corresponding author: norakmal@utm.my**

ISSN: 1823-7010, eISSN: 2600-7444

1. INTRODUCTION

Global energy demand continues to rise annually. Despite the rapid expansion of renewable generation, fossil fuels remain the dominant energy source. Achieving carbon neutrality will require not only scaling renewable technologies but also developing safe, cost-effective and sustainable energy storage systems. Lithium-ion batteries currently dominate the electrochemical storage market due to their high energy density [1]. However, their long-term viability is constrained by the scarcity and rising cost of lithium resources, as well as safety risks associated with flammable electrodes [2]. These limitations restrict their suitability for grid-scale deployment and highlight the urgent need for alternative battery technologies that are both sustainable and reliable. Therefore, Zn-ion batteries have emerged as one of the most promising candidates.

Zn metal is naturally abundant, inexpensive and environmentally benign, while its use with aqueous alkaline electrolytes provides intrinsic safety benefits [3]. In principle, Zn anodes offer high theoretical capacity and stable redox chemistry, making them highly attractive for large-scale energy storage [4]. Nevertheless, the practical application is hindered by sluggish electrochemical kinetics. Conventional planar Zn anodes, with their limited surface area, suffer from poor ion transport, high polarization and accelerated degradation, which compromise efficiency and cycle life [5]. Previous research efforts have always focused on the development of cathode materials and electrolytes, while comparatively little attention has been given at the anode side. In Zn-ion battery systems, the mass of Zn anode is far greater than necessary to balance the capacity of cathode [6]. Moreover, the surface-active Zn on the anode participates directly in redox reactions during charge-discharge process. Therefore, advanced design of Zn anode is critical for enhancing electrochemical performance.

Prior studies have demonstrated the potential of combining surface chemistry with microstructural engineering. Zhu et al. [7] reported enhanced reversibility in surface-alloyed nanoporous Zn, while Meng et al. [8] developed a self-supported lamellar nanoporous copper heterostructure anode to regulate Zn electrochemical activity. The alternating layered channels promote homogeneous ion transport and the open porous architecture provides large surface area for electrochemical stability. Mohd Shumiri et al. [9] agreed that porous lamellar design offers exceptional uniformity with precisely aligned channels. These characteristics make lamellar porous Zn anodes compelling candidates for stable and efficient Zn-based electrodes. Additionally, Xu et al. [10] achieved stable Zn deposition by dispersing Sb nanoparticles on a 3D copper substrate, whereas Hong et al. [11] modified Zn plate anode with a thin metallic Sb layer, promoting stronger Zn-ion interaction and reduced nucleation overpotential even at high current density. The incorporation of Sb reduces the electrolyte contact angle, indicating improved wettability that promotes uniform dispersion of the electrolyte across the surface. Furthermore, the high surface free energy of Sb facilitates homogeneous distribution of Zn-ions, thereby enhancing Zn deposition behavior [12]. However, significant opportunities remain. Despite these distinct advantages, studies on antimony modification in porous lamellar zinc alloys remain limited.

Therefore, the present study seeks to address this gap by introducing a novel strategy that integrates lamellar porous Zn with Sb modification to enhance electrochemical performance in alkaline aqueous electrolytes. The tailored lamellar architecture promotes uniform ion transport, while Sb incorporation improves reaction kinetics and regulates Zn nucleation. This work demonstrates a simple and scalable approach for engineering high-performance Zn anodes and provides valuable insights for advancing next-generation aqueous Zn-based energy storage systems.

2. MATERIALS AND METHODS

2.1 Preparation of Sb-pZn anode

Zn-5Al (wt.%) precursor alloy was first prepared by induction melting of high-purity Zn (99.99 %) and Al (99.99 %) in alumina crucible, followed by solidification under controlled cooling conditions (water-, air- and furnace-cooled). After complete solidification, the ingot was removed from the crucible and sectioned into 10 mm × 10 mm × 1 mm alloy sheets using precision cutter. The Zn-5Al sheets were then chemically dealloyed to prepare porous lamellar Zn (pZn), in which the less noble Al component was selectively dissolved in 4 M NaOH solution at 50 °C for 4 h as reported in our previous work [13]. After thorough rinsing with pure water and ethanol, the pZn sheets were immersed in 0.15 M $SbCl_3$ solution for 3 minutes at room temperature to obtain Sb-modified porous lamellar Zn (Sb-pZn) via galvanic replacement reaction. In this process, Zn was oxidized to Zn^{2+} while Sb^{3+} was reduced and deposited as metallic Sb ($3Zn + 2SbCl_3 \rightarrow 3ZnCl_2 + 2Sb$). The as-prepared Sb-pZn sheets were subsequently washed with ethanol to remove residual chemicals from the pore channels and directly used as electrodes for electrochemical testing.

2.2 Materials characterization

Electron micrographic analysis was performed using variable-pressure scanning electron microscope (VPSEM, Zeiss Supra VP35) equipped with energy-dispersive X-ray spectroscopy (EDS) for elemental analysis. Samples were mounted on aluminium stubs with conductive carbon tape and placed in the chamber under vacuum to minimize interference. An acceleration voltage of 15 kV was applied and SEM images were captured at various magnifications along with corresponding EDS elemental mappings. X-ray diffraction (XRD) analysis was carried out using Rigaku SmartLab2018 diffractometer with Cu Kα radiation ($\lambda = 1.5406$ Å). Diffraction data were collected over 2θ range of 20°-100° with scanning speed of 2° per minute and step size of 0.02°. The diffraction patterns were analyzed using X'Pert HighScore Plus program and compared with standard reference data from the International Centre for Diffraction Data (ICDD) database for phase identification and structural analysis.

2.3 Electrochemical measurements

Electrochemical properties were measured using potentiostat-galvanostat (Gamry 1010B) in three-electrode system. The as-prepared Sb-pZn, pZn and bare Zn samples were used as working electrodes, 10 mL of 8.5 M KOH and 0.6 M ZnO solution as the electrolyte, graphite rod as the counter electrode and Ag/AgCl (3 M KCl) as the reference electrode. Cyclic voltammetry (CV) was performed to evaluate Zn oxidation and reduction behavior, with initial potential of 0 V, switching potential of -2.0 V and scan rates ranging from 10 mV/s to 50 mV/s. Current density versus voltage curves were obtained to observe the redox peaks corresponding to Zn stripping (oxidation) and plating (reduction). Zn^{2+} diffusion coefficient was calculated using Randles-Sevcik Equation 1 [14],

$$i_p=\left(2.68648\times10^5\right)n^{3/2}AD_o^{1/2}C_o v^{1/2} \tag{1}$$

where i_p is the peak current, n is the number of electrons involved in the reaction (assumed to be 2), D is the apparent ion diffusion coefficient, C is the concentration of Zn^{2+} in the electrolyte, A is the effective electrode area and ν is the scan rate. Electrochemical impedance spectroscopy (EIS) was conducted to evaluate Zn ion transfer kinetics by applying 10 mV AC voltage signal over frequency range of 10 kHz to 0.1 Hz. The impedance response was analyzed using Nyquist and Bode plots. The solution resistance, R_s represents the intrinsic resistance of both electrolyte and electrode. Meanwhile, the charge transfer resistance, R_{ct} is associated with electron transfer kinetics at the electrode. At high frequency, intercept of EIS spectra with the real part corresponds to R_s. In middle frequency range, the semicircle diameter reflects the parallel connection of R_{ct} and constant phase element, CPE. The plots at low frequency represents Warburg resistance, Z_w. Based on the equivalent circuit, EIS spectra were analyzed using complex nonlinear least squares fitting. All spectra were fitted using Z-view software. Chronopotentiometry was conducted to evaluate nucleation overpotential by measuring voltage as a function of time at constant current density of 0.2 mA/cm^2.

3. RESULTS AND DISCUSSION

3.1 Morphological and structural characteristics of Sb-pZn

3.1.1 SEM and EDS analysis

As shown in Figure 1, the lamellar-structured Zn-Al alloy was first fabricated by induction melting of pure Zn and Al at the eutectic composition, followed by chemical dealloying and surface modification process meanwhile Figure 2 shows microstructural properties of the modified Zn anode.

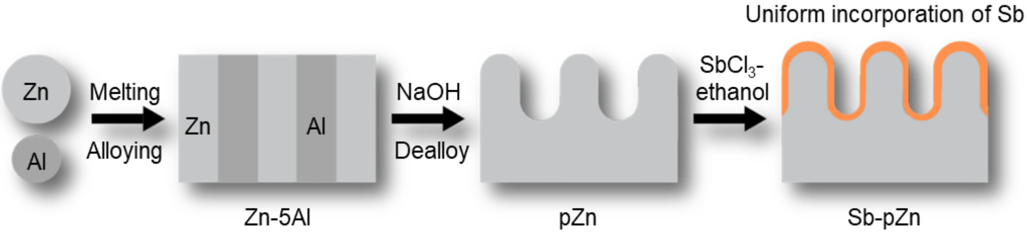

Figure 1: Schematic illustration of Sb-pZn fabricated by alloying-dealloying of Zn-Al, followed by surface modification with Sb on the porous lamellar structure

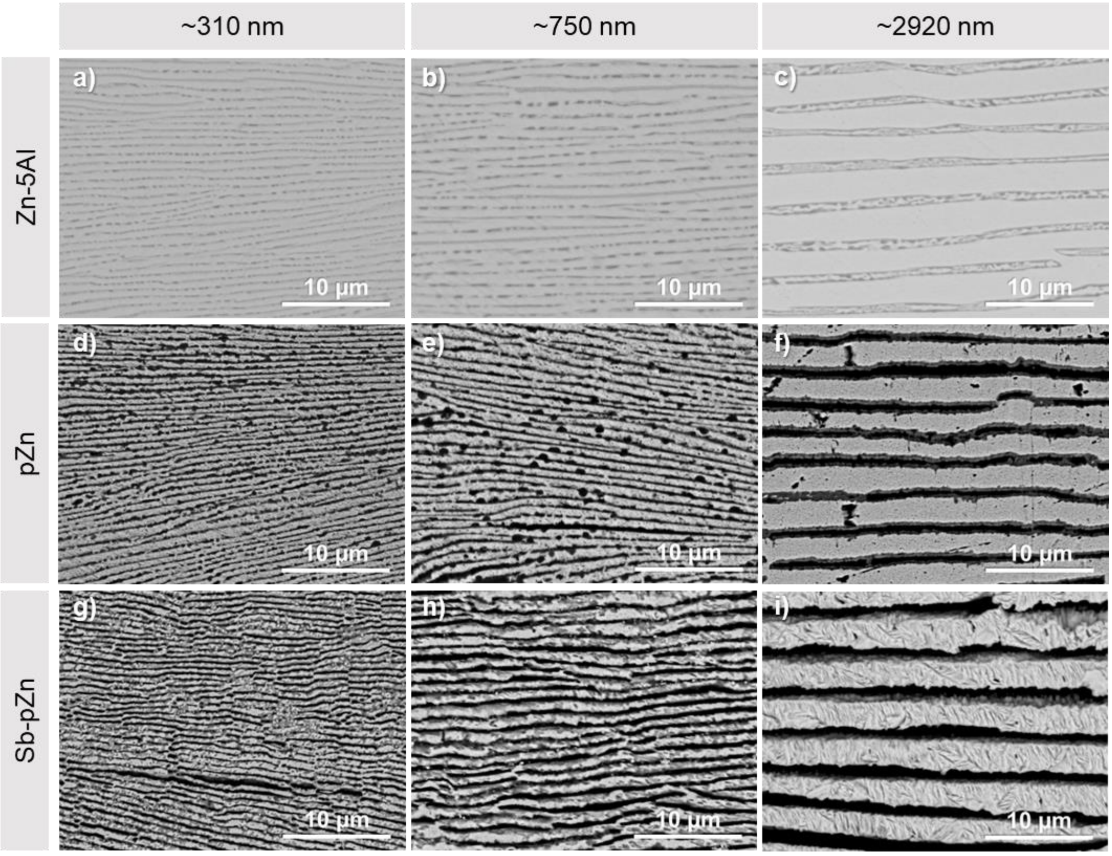

Figure 2: Microstructural properties of the modified Zn anode (a-c) SEM images of eutectic Zn-5Al precursor alloy prepared by induction melting of high-purity Zn and Al. (d-f) SEM images of dealloyed pZn obtained by chemical dealloying in NaOH solution. (g-i) SEM images of Sb-pZn showing metallic Sb deposited on the porous Zn lamellar by galvanic replacement reaction. Surface modification of pZn with Sb was achieved by simple chemical displacement reaction.

The precursor alloy was solidified under controlled cooling conditions, producing Zn lamellae with thicknesses of ~310 nm in water-cooled (Figure 2(a)), ~750 nm in air-cooled (Figure 2(b)) and ~2920 nm in furnace-cooled (Figure 2(c)). Chemical dealloying in NaOH solution selectively dissolved the Al component, creating aligned channels and resulting in highly ordered lamellar porous structure. SEM images of the dealloyed pZn (Figures 2(d-f)) clearly reveal lamellar porous architecture consisting of quasi-periodic channels and Zn ligaments. SEM micrographs in Figures 2(g-i) confirmed the uniform deposition of Sb, forming a textured layer across the freestanding pZn framework while maintaining the underlying lamellar porosity.

EDS elemental mapping in Figures 3(a-c) further validated the uniform distribution of Sb. This demonstrates the compatibility of modification process with the Zn lamellar substrate.

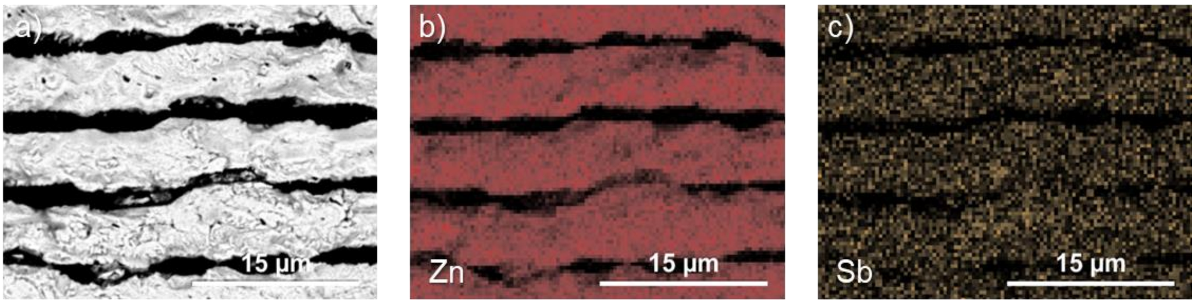

Figure 3: EDS analysis of Sb-pZn-2920. (a) SEM image with corresponding elemental mappings of (b) Zn and (c) Sb

3.1.2 XRD analysis

Crystalline structure and phase composition of Sb-pZn were characterized by XRD. The diffraction patterns in Figures 4(a) and (b) confirmed the coexistence of metallic Zn and Sb, with characteristic peaks corresponding to hexagonal Zn (JCPDS 04-0831) and hexagonal Sb (JCPDS 35-0732).

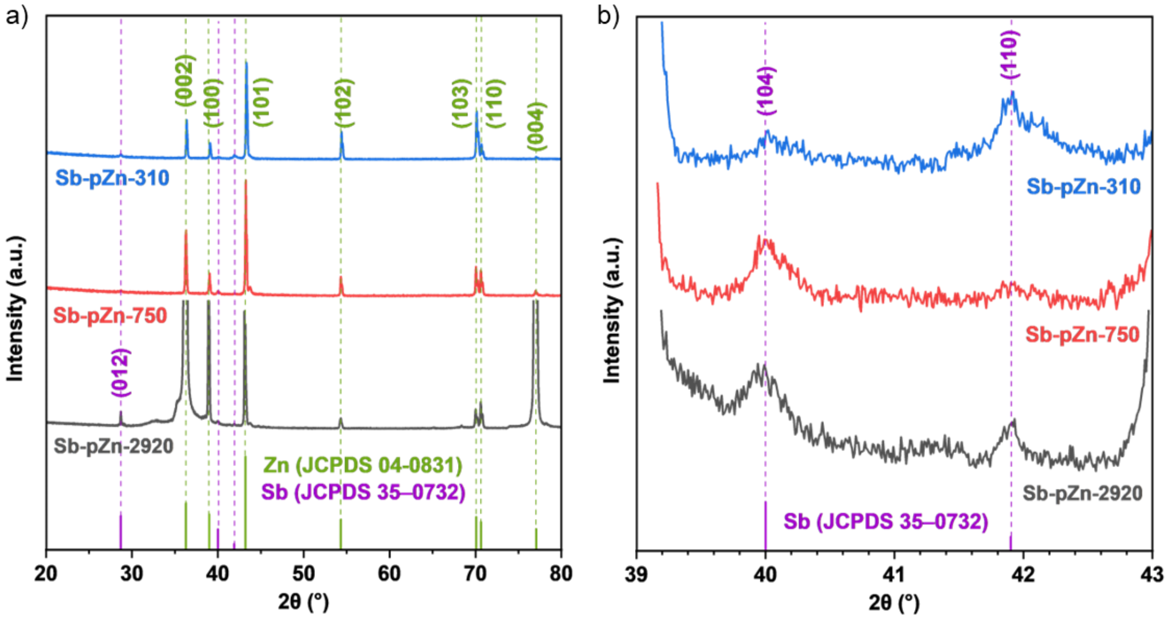

Figure 4: XRD analysis of the modified Zn anode. (a) Diffraction patterns and (b) the enlarged view showing the minor peaks of hexagonal Sb

The minor peaks at 28.7°, 40.0° and 41.9° are indexed to (012), (104) and (110) planes of hexagonal Sb, confirming successful incorporation of Sb onto the pZn surface. Meanwhile, the major peaks at 36.34°, 39.06°, 43.31°, 54.38°, 70.11°, 70.68° and 77.01° are attributed to (002), (100), (101), (102), (103), (110) and (004) planes of hexagonal Zn, respectively.

3.2 Electrochemical performance

To evaluate the electrochemical behavior, CV measurements were conducted in three-electrode system. As shown in Figure 5(a), all samples were preconditioned for 10 cycles to achieve stable electrochemical response. The potential was first scanned in reverse from 0 V to -2.0 V vs. Ag/AgCl followed by forward scan from -2.0 V to 0 V at scan rate of 10 mV/s. In forward scan, anodic peak corresponding to Zn oxidation was observed. This process involves dissolution of metallic Zn into Zn^{2+}, which subsequently reacts with hydroxide ions (OH^-) to form $Zn(OH)_2$. Further interaction with OH^- produces soluble zincate ions ($(Zn(OH)_4)^{2-}$). As the zincate concentration reaches solubility limit, ZnO precipitates on the electrode surface, gradually forming passive layer that impedes further Zn dissolution [15]. The formation of ZnO layer contributes to notable decrease in current, as the reaction rate becomes limited by the diffusion of OH^- ions to the electrode interface [16].

From Figure 5(b), the shift in oxidation peak potential shows different Zn dissolution behavior. The peak for bare Zn appeared at -0.491 V, whereas for pZn-2920 it shifted to -0.638 V. Sb-pZn-2920 showed even larger shift to -0.765 V, indicating better Zn dissolution kinetics. The incorporation of Sb successfully modifies the electronic structure which facilitates Zn oxidation at lower overpotentials. Additionally, it showed stronger anodic peak current densities (0.355 A/cm^2) that indicate efficient zincate ion formation in the forward scan.

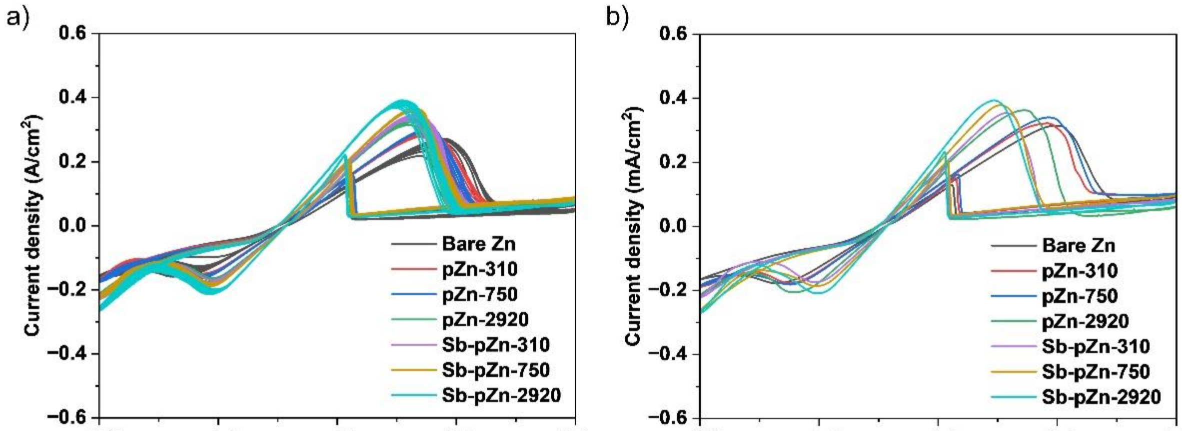

Figure 5: CV curves of bare Zn and the modified Zn anode in KOH-ZnO electrolyte over the potential range of 0 to -2.0 V vs. Ag/AgCl at scan rate of 10 mV/s for (a) 10 pre-conditioning cycles and (b) one cycle

In reverse scan, additional sharp oxidation peak appeared that attributed to the re-establishment of Zn oxidation process following the partial removal of ZnO layer. As previously reported, this peak corresponds to the breakdown of accumulated ZnO on the electrode surface, allowing Zn to undergo oxidation once again [17]. The reaction can be expressed as $ZnO + H_2O + 2OH^- \rightarrow Zn(OH)_4^{2-}$. This peak reflects the re-oxidation of Zn in the presence of pre-formed oxide layers, confirming the transient nature of ZnO passivation. The gradual removal of ZnO exposes fresh Zn to enable renewed oxidation. So, additional unreacted Zn surfaces become available to the electrolyte, resulting in instantaneous increase in current. On top of that, cathodic peak that correspond to reduction of zincate ions to metallic Zn was observed. Bare Zn shows reduction peak at -1.674 V while pZn-2920 shifts to -1.601 V. The greater shift is observed for Sb-pZn-2920 at -1.501 V that indicates lower energy barrier for Zn deposition which can be attributed to improved nucleation kinetics. Additionally, stronger cathodic peak current density further confirms the enhanced reduction activity. Sb-pZn-2920 demonstrated slightly higher current at 0.204 A/cm^2. These results emphasize the positive effects of both porosity and Sb incorporation in enhancing the reduction behavior.

Apart from that, smaller peak-to-peak separation (ΔE_p) indicates improved charge transfer kinetics of redox couple. Bare Zn shows large ΔE_p (1.183 V) that suggests sluggish kinetic and high polarization loss. In contrast, pZn-2920 demonstrated decrease in ΔE_p (0.963 V), reflecting enhanced reaction dynamics. The more pronounced improvement was observed in Sb-pZn-2920 where ΔE_p further decreased to 0.736 V. This reduction shows superior charge transfer kinetic and lower polarization loss. Also, the results suggested that lamellar thickness plays significant role in the reaction mechanism. A clear correlation is observed where larger lamellae deliver better performance due to more developed porous structure, resulting in increased surface area that enables more active electrochemical reactions, while the introduction of Sb further enhances interfacial reaction kinetics [13]. Table 1 summarizes all parameters obtained from CV measurement.

Table 1: Electrochemical parameters obtained from CV measurements

Electrode	Oxidation peak		Reduction peak		ΔEp (V)
	Potential (V)	Current (A/cm^2)	Potential (V)	Current (A/cm^2)	
Bare Zn	-0.491	0.252	-1.674	0.161	1.183
pZn-310	-0.537	0.245	-1.617	0.172	1.080
pZn-750	-0.544	0.263	-1.620	0.174	1.075
pZn-2920	-0.638	0.308	-1.601	0.195	0.963
Sb-pZn-310	-0.716	0.316	-1.512	0.171	0.796
Sb-pZn-750	-0.736	0.337	-1.507	0.183	0.771
Sb-pZn-2920	-0.765	0.355	-1.501	0.204	0.736

As shown in Figure 6(a-c), increasing the scan rate from 10 to 50 mV/s causes ΔE_p to widen. This indicates that the electrode reaction is limited by diffusion and charge transfer resistance. At higher scan rates, the electron transfer timescale is reduced and result in sluggish charge transfer. Consequently, cathodic peak shifts to higher potential as the reduction process requires additional energy to compensate for slower ion transport [18]. Similarly, the anodic peak shifts due to delayed oxidation kinetics. To evaluate diffusion behavior, the current density evolution at varied scan rates was analyzed. Zn^{2+} diffusion coefficient was calculated using Randles-Sevcik equation (1). Linear plots of peak current versus the square root of scan rate were presented in Figure 6(d-e). Sb-pZn-2920 shows high diffusion coefficient for oxidation (1.10×10^{-5} cm^2/s) and reduction (1.16×10^{-5} cm^2/s), indicating better ion transport.

As CV lacks direct measurement of resistance, EIS was conducted to quantitatively analyze the solution resistance, R_s and charge transfer resistance, R_{ct}. Nyquist plots show single semicircle across the high to low frequency range (Figure 7(a)). Bare Zn shows high R_s (2.215 Ω) due to low wettability on the planar surface structure. In contrast, Sb-pZn-2920 shows lower R_s (0.882 Ω) as the porous lamellar structure improved electrolyte interaction. The highly uniform lamellar channels improve liquid-solid interaction as the confined space within the pores enhances electrolyte penetration and distribution.

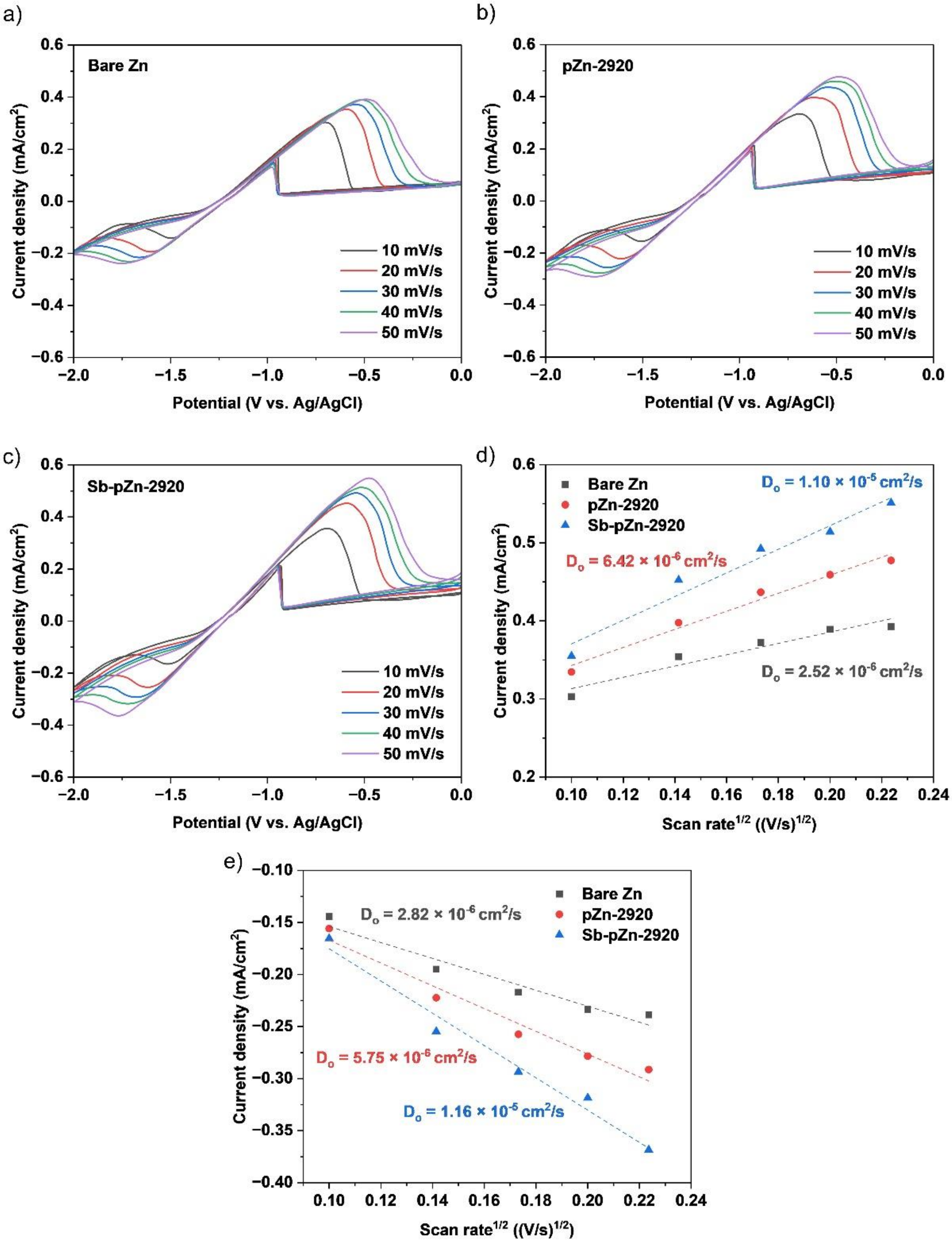

Figure 6: CV curves at scan rate ranging from 10 to 50 mV/s for (a) bare Zn, (b) pZn-2920 and (c) Sb-pZn-2920. Randles-Sevcik plots of (d) anodic and (e) cathodic peak current density as a function of the square root of the scan rate

Additionally, Sb modification promotes better electrolyte adhesion that reduce contact resistance between electrolyte and electrode. Furthermore, bare Zn shows high R_{ct} (4.238 Ω) that indicates high resistance to Zn ion transfer at the interface. The planar surface causes localized reaction which increases interface irregularity and hinders electron flow [19]. In contrast, Sb-pZn-2920 achieves lower R_{ct} (1.770 Ω). This reduction confirms faster Zn ion transfer and improved reaction kinetics which is consistent with CV analysis. The modified Zn anode become more conducive to electron transfer. Observed carefully, larger lamellar pore results in lower R_{ct}. The larger lamellar channel creates more open pathways for electrolyte penetration and accessibility [12].

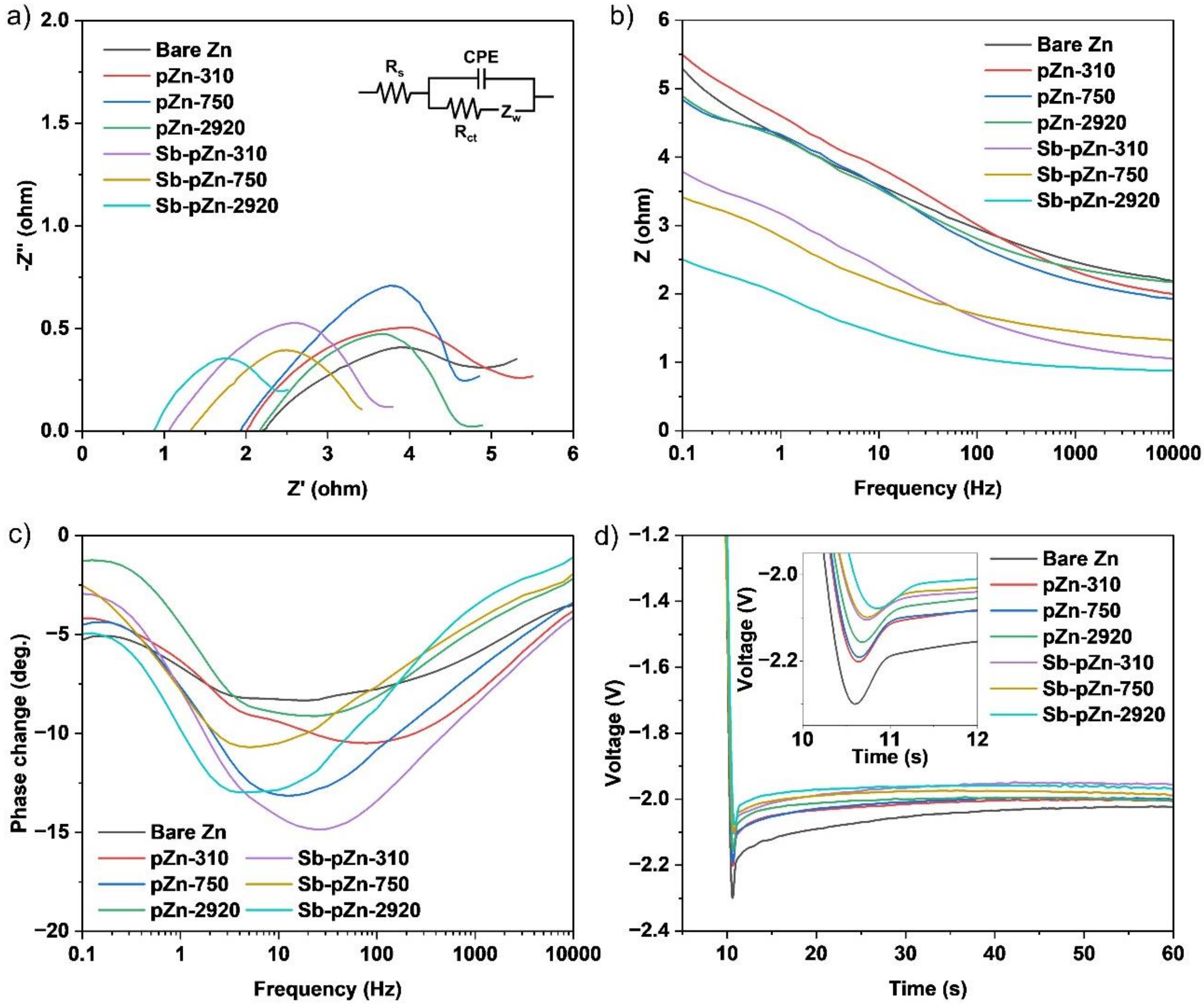

Figure 7: Electrochemical properties of bare Zn and the modified Zn anodes. (a) Nyquist plots, (b) Bode plots of log |Z| vs. log frequency, (c) Bode plots of phase angle vs. log frequency and (d) voltage-time profiles at current density of 0.2 mA/cm^2

Apart from that, R_{ct} and R_s were analyzed by Bode plots of impedance (Z) as a function of logarithmic frequency (Figure 7(b)). The low frequency region represents charge transfer process while the high frequency region dominated by solution resistance. Consistently, Sb-pZn-2920 showed the lowest impedance plot which indicates faster charge transfer kinetics. Similarly, in high frequency region, Sb-pZn-2920 demonstrated the lowest impedance magnitude that suggests improved electrode-electrolyte resistance while bare Zn had the highest impedance due to poor wettability and higher interfacial resistance. From Figure 7(c), the single peak was observed in the Bode phase angle plot across all samples which corresponds to single loop in Nyquist plot. This confirms the presence of one dominant time constant in the equivalent circuit. Most importantly, the increase in phase angle at relaxation frequency was obviously observed that indicates enhanced capacitive response compared to bare Zn.

As shown in Figure 7(d), chronopotentiometry was conducted to further confirm the Zn deposition behavior. Bare Zn shows large nucleation overpotential of 278.1 mV with steady-state potential of -2.022 V. This indicates limitation of planar structure in promoting efficient Zn deposition. In contrast, pZn-2920 achieves lower overpotential (156.2 mV), confirming that the porous structure provides better electroactive surface exposure that promotes deposition kinetics. Additionally, the integration of Sb further enhances the interfacial interactions. Sb-pZn-2920 shows further reduction in both nucleation (101.3 mV) and plateau overpotentials (1.962 V). This improvement is directly related to the synergistic effect of Sb component and porous lamellar architecture which creates abundant active sites for more efficient Zn nucleation and growth. Consistently, greater lamellar pores result in lower overpotential, and this trend remains consistent before and after modification. The larger lamellar network enhances electronic conductivity, while Sb incorporation effectively regulates Zn nucleation. Moreover, the alternating stacked lamellar structure with more open channels provides higher surface area, thereby promoting improved Zn deposition behavior [13].

4. CONCLUSIONS

In summary, a newly designed Sb-pZn has been successfully engineered as high-performance anode for alkaline aqueous Zn-based energy storage systems. The combination of lamellar framework with Sb creates highly conducive surface that facilitates efficient Zn^{2+} ion transport and accelerates electrochemical reactions. As a result, Sb-pZn shows superior Zn oxidation and reduction behavior characterized by low polarization. Chronopotentiometry analysis demonstrates low nucleation overpotential (101.3 mV) under high current density of 1 mA/cm^2, outperforming the unmodified bare Zn electrode. CV analysis reveals better redox kinetics with stronger peaks and reduced peak separation, indicating faster electron and ion transfer. EIS analysis confirms these findings, showing substantial reduction in R_{ct} (1.770 Ω), reflecting the improved interfacial dynamics. The combined effects between porous lamellar architecture and Sb modification provides robust strategy to overcome the persistent challenges of planar Zn anodes. Importantly, this approach not only enables the design of stable Zn anodes but also establishes a broadly applicable methodology for tailoring surface chemistry and microstructure in metal-based electrodes. These findings represent significant step forward in advancing safe, durable and high-rate aqueous Zn energy storage systems, bridging the gap toward their practical deployment in large-scale energy applications.

Acknowledgements

This work was financially supported by the Universiti Teknologi Malaysia under the grant scheme of UTM Fundamental Research (Q.J130000.3824.23H15). We thank the Materials Research and Consultancy Group, Faculty of Mechanical Engineering, Universiti Teknologi Malaysia for the research support towards this publication.

Author Contributions

All authors contributed toward data analysis, drafting and critically revising the paper and agree to be accountable for all aspects of the work.

Disclosure of Conflict of Interest

The authors have no disclosures to declare.

Compliance with Ethical Standards

The work is compliant with ethical standards.

References

[1] Ngoy, K.R., Lukong, V.T., Yoro, K.O., Makambo, J.B., Chukwuati, N.C., Ibegbulam, C., Eterigho-Ikelegbe, O., Ukoba, K. and Jen, T.-C. (2025). Lithium-ion batteries and the future of sustainable energy: A comprehensive review. *Renewable and Sustainable Energy Reviews*. 223, 115971.

[2] Ramasubramanian, B., Ling, J., Jose, R. and Ramakrishna, S. (2024). Ten major challenges for sustainable lithium-ion batteries. *Cell Reports Physical Science*. 5(6), 102032.

[3] Liu, Y., Lu, X., Lai, F., Liu, T., Shearing, P.R., Parkin, I.P., He, G. and Brett, D.J.L. (2021). Rechargeable aqueous Zn-based energy storage devices. *Joule*. 5(11), 2845-2903.

[4] Chen, Q., Jiang, C., Chen, M., Zhang, J., Hou, G. and Tang, Y. (2022). Magnetic field stabilizes zinc anode. *Surfaces and Interfaces*. 31.

[5] Alemu, M.A., Worku, A.K. and Getie, M.Z. (2024). Recent advances in electrically rechargeable transition metal-based-air batteries for electric mobility. *Inorganic Chemistry Communications*. 159.

[6] Zhu, C., Li, P., Xu, G., Cheng, H. and Gao, G. (2023). Recent progress and challenges of Zn anode modification materials in aqueous Zn-ion batteries. *Coordination Chemistry Reviews*. 485, 215142.

[7] Zhu, K., Lei, Z., Hu, M., Qu, Z., Lyu, S.-S. and Mo, D.-C. (2026). Hexagonal Porous Zincophilic Alloy Interface for Ultrastable Zinc Metal Anode. *Applied Materials & Interfaces*. 18(6), 9963-9973.

[8] Meng, H., Ran, Q., Dai, T.-Y., Jia, J.-H., Liu, J., Shi, H., Han, G.-F., Wang, T.-H., Wen, Z., Lang, X.-Y. and Jiang, Q. (2024). Lamellar Nanoporous Metal/Intermetallic Compound Heterostructure Regulating Dendrite-Free Zinc Electrodeposition for Wide-Temperature Aqueous Zinc-Ion Battery. *Advanced Materials*. 36(26), 2403803.

[9] Mohd Shumiri, M.A.I., Mohd Najib, A.S., Putra, A.E.E. and Fadil, N.A. (2025). Electrochemical and chemical dealloying of nanoporous anode materials for energy storage applications. *Science and Technology of Advanced Materials*. 26(1), 2451017.

[10] Xu, K., Zheng, X., Luo, R., Sun, J., Ma, Y., Chen, N., Wang, M., Song, L., Zhao, Q. and Chen, W. (2023). A three-dimensional zincophilic nano-copper host enables dendrite-free and anode-free Zn batteries. *Materials Today Energy*. 34.

[11] Hong, L., Wang, L.Y., Wang, Y., Wu, X., Huang, W., Zhou, Y., Wang, K.X. and Chen, J.S. (2022). Toward Hydrogen-Free and Dendrite-Free Aqueous Zinc Batteries: Formation of Zincophilic Protective Layer on Zn Anodes. *Advanced Science*. 9(6), e2104866.

[12] Mohd Shumiri, M.A.I., Mohd Najib, A.S. and Fadil, N.A. (2025). Current status and advances in zinc anodes for rechargeable aqueous zinc-air batteries. *Science and Technology of Advanced Materials*. 26(1), 2448418.

[13] Mohd Shumiri, M.A.I., Mohd Najib, A.S. and Fadil, N.A. (2025). Fabrication of uniform porous lamellar zinc structures by dealloying of eutectic binary zinc-aluminium alloys. *Malaysian Journal of Microscopy*. 21(1), 34-46.

[14] Song, Z., Wang, B., Zhang, W., Zhu, Q., Elezzabi, A.Y., Liu, L., Yu, W.W. and Li, H. (2023). Fast and Stable Zinc Anode-Based Electrochromic Displays Enabled by Bimetallically Doped Vanadate and Aqueous Zn(2+)/Na(+) Hybrid Electrolytes. *Nano-Micro Letters*. 15(1), 229.

[15] Wang, T., Kunimoto, M., Yanagisawa, M., Morita, M., Abe, T. and Homma, T. (2024). Zn Dissolution−Passivation Behavior with ZnO Formation via In Situ Characterizations. *Energy & Environmental Materials*. 7(1), e12481.

[16] Guo, X., Zhang, S., Hong, H., Wang, S., Zhu, J. and Zhi, C. (2025). Interface regulation and electrolyte design strategies for zinc anodes in high-performance zinc metal batteries. *iScience*. 28(2), 111751.

[17] Rodriguez Lopez, J.C., Vigueras Santiago, E., García-González, N., Castrejón-Sánchez, V.H., Camacho-López, M. and Hernández López, S. (2026). Study of the phase composition (Zn, ZnO) of anodes recovered from spent alkaline batteries, with respect to their residual voltage. *Waste Management Bulletin*. 4(1), 100281.

[18] Kim, A., Kim, H. and Nam, K.W. (2025). Achieving superior stability and cycle life in zinc anodes with aramid surface modification. *Journal of Materials Chemistry A*. 13(35), 29109-29119.

[19] Huang, H., Xu, J., Huang, Y., He, Z., Feng, H., Hu, C., Chen, Z., Yang, Z., Tian, T. and Zhang, W. (2024). Adjusting Interface Dynamics: A New Insight into the Role of Electrolyte Additive in Facilitating Highly Reversible (002)-Textured Zinc Anode at High Current and Areal Densities. *Advanced Energy Materials*. 14(41), 2401643.